Construction and Building Materials 236 (2020) 117559

Contents lists available at ScienceDirect

Construction and Building Materials

journal homepage: www.elsevier.com/locate/conbuildmat

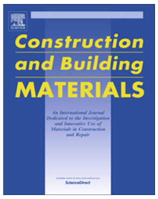

Effect of TiO_2 and fly ash on photocatalytic NO_x abatement of engineered cementitious composites

Mingfeng Xu [a,b,c], Herek Clack [c], Tian Xia [c], Yi Bao [c], Kai Wu [b], Huisheng Shi [b], Victor Li [c,*]

[a] School of Civil and Transportation Engineering, Hebei University of Technology, Tianjin 300401, China
[b] School of Materials Science and Engineering, Tongji University, 4800 Caoan Road, Shanghai 201804, China
[c] Department of Civil and Environmental Engineering, University of Michigan, Ann Arbor, MI 48109-2125, USA

HIGHLIGHTS

- TiO_2 in ECC is effective in NO_x abatement.
- Increasing fly ash content is found to enhance the NO_x abatement rate and efficiency.
- The improvement in NO_x abatement rate and efficiency is related to microstructure modification.
- A first-order reaction model can effectively capture the NO_x abatement through PC reactions.

ARTICLE INFO

Article history:
Received 1 March 2019
Received in revised form 2 September 2019
Accepted 8 November 2019

Keywords:
Titanium dioxide (TiO_2)
Air purifying
Engineered Cementitious Composites (ECC)
Fly ash
Nitrogen oxides (NO_x) abatement
Photocatalytic

ABSTRACT

Titanium dioxide (TiO_2) nanoparticles have been incorporated in cementitious composites to achieve photocatalytic (PC) functions such as self-cleaning and air purifying functions. This study experimentally investigates the effect of TiO_2 nanoparticles and fly ash on the nitrogen oxides (NO_x) abatement rate and efficiency of Engineered Cementitious Composites (ECC) that has retained strain-hardening properties and tensile ductility. Emphasis is placed on understanding the fundamental mechanisms through research on the microstructures and chemical environment of the composite material. A first-order chemical reaction model is applied to analyze the PC reaction rate and residual NO_x concentration. Test results indicate that the PC reaction rate and efficiency increase with the TiO_2 content from 0 to 5%, and the fly ash to cement ratio from 0 to 2.2. Using the low-calcium fly ash further increases the PC reaction rate and efficiency. The microstructure change originated from different fly ash contents and types are closely related to PC efficiency changes. This study advances the fundamental knowledge for engineering the cementitious composites to achieve the optimal PC functions.

1. Introduction

Due to rapid industrialization and urbanization, air pollution has become a major concerning issue modern society faces. In particular, it is known that fine particles smaller than 2.5 μm ($PM_{2.5}$) adversely affect human health [1]. According to the annual report of State of Global Air 2018, about 95% of the world's population live in areas where the $PM_{2.5}$ exceeds the World Health Organization's Air Quality Guideline (10 $\mu g/m^3$) [2]. $PM_{2.5}$ enters the atmosphere from primary emissions and is also produced in the atmosphere from reactions of gaseous precursors, the latter being the major contributor to the total $PM_{2.5}$ mass [3]. Therefore, the gaseous precursors, especially nitrogen oxides (NO_x), are closely associated with air pollution. Reducing NO_x concentration has become a key task in the control of air pollution and reducing environmental, economic and health costs [4].

As one of the most widely used construction materials, concrete has attracted increasing interest for the potential ability of the resulting concrete structures to passively purify the air. Titanium dioxide (TiO_2) has been used as a photocatalyst in developing photocatalytic (PC) concrete with embodied functionality for pollutant abatement. In PC concrete, TiO_2 particles are incorporated as an additive to stimulate PC reactions [5,6]. When PC concrete is exposed to ultraviolet (UV) irradiation, TiO_2 absorbs photon energy to overcome the energy band gap and promote electrons from the valence band to the conduction band [7]. The activation of the electrons produces 'holes' (electron vacancy) in the valence band, generating highly active hydroxyl radicals ($\cdot OH$) that oxidize NO_x and produce nitric acid (HNO_3) [8,9]. The PC reactions primarily occur

---

[*] Corresponding author.
E-mail address: vcli@umich.edu (V. Li).

https://doi.org/10.1016/j.conbuildmat.2019.117559

at the interface between air and the PC concrete where NO_x molecules in air are in contact with the highly active hydroxyl radicals produced by UV radiation incident on the concrete surface. Both laboratory and field tests have shown promise of PC concrete pavement in reducing NO_x [10–14]. 36.7%–82.0% NO_x was reported to be abated by TiO_2 panels in an artificial street canyon in France [13]. Under ideal environmental conditions (high radiation and low relative humidity), NO_x abatement up to 45% was observed in a TiO_2-street in the Netherlands [14].

The PC efficiency for NO_x abatement is dependent on the microstructure of the TiO_2-doped cementitious composites [10,15–17]. Sugrañez et al. [16] claimed that the PC efficiency increased with the porosity of the host matrix [16], because the PC reactions occur at the surfaces where there are active hydroxyl radicals [8,18]. The increase of porosity leads to a larger surface to volume ratio, providing a larger surface area for the PC reactions. In this sense, concrete is advantageous as the host material for TiO_2, because its porous microstructure provides an enlarged surface area that facilitates the production of hydroxyl radicals and contact between NO_x and the hydroxyl radicals [19]. However, Lucas et al. argued that a high porosity did not necessarily lead to a high PC efficiency, and stated that the pore size distribution of the matrix had significant effect on the PC efficiency [10]. It was reported that finer pores (less than 0.1 μm) did not help improve the NO_x abatement efficiency [10]. This was attributed to the limited accessibility of water and NO_x to the fine pores, limiting the exposure of NO_x to active hydroxyl radicals. The above studies suggest that the NO_x abatement efficiency is associated with the microstructure characteristics of the host matrix. In addition, the NO_x abatement efficiency is dependent on the chemical environment of the matrix. When TiO_2-doped glass [20] and alumina [21] were exposed to UV light and NO_x, the NO_x abatement reactions were exhausted after a period of exposure, due to the accumulation of HNO_3 that inhibits continued reactions [22]. In this sense, an alkaline matrix helps consume HNO_3, thus promoting the PC reactions [17,23]. Horgnies et al. found that concrete by itself (without TiO_2) can absorb 40–80% NO_2 over 20 h continuous flow test with a constant flow of 250 ppb NO_2 (effective volume/surface ratio:17.3 cm) [24]. This is consistent with the expected reaction between NO_x and strong alkaline hydrates of cementitious materials [25].

Although PC concrete has been proven promising for air purification in pavement applications, conventional concrete is brittle and fractures suddenly under tension. For structures that require tensile resistance, Engineered Cementitious Composites (ECC) is known to have outstanding crack resistance, superior tensile ductility (3% to 7%), and autogenous crack width control (about 60 μm) [26]. ECC has been applied in various civil infrastructure applications including buildings, bridges, etc. and demonstrated greatly improved safety, durability, and sustainability [27,28]. A self-cleaning ECC was developed by incorporating TiO_2 for removal of dirt or stains [29]. Typically, ECC is prepared using high-volume by-products, such as fly ash (up to 85 wt% of the binder) [30–32]. The fly ash may change the pore characteristics [33] and pH value of pore solution [34,35], thus modifying the PC efficiency. To date, there is a lack of knowledge on the effect of fly ash on the PC efficiency. The air purifying functionality of TiO_2-doped ECC has not been previously studied.

This research aims to understand the effect of TiO_2 nanoparticles and fly ash on the NO_x abatement efficiency of PC-ECC. To this end, ECC specimens with different amounts of TiO_2 nanoparticles and fly ash were tested; two types of fly ash with different chemical compositions were investigated. A first-order chemical reaction model is used to analyze the PC reactions, and to evaluate the effect of TiO_2 and fly ash on the NO_x abatement efficiency based on the experimental results. The underlying fundamental mechanisms are investigated from the perspectives of TiO_2 dispersion, pore structure, and pH of the pore solution.

2. Experimental program

2.1. Raw materials and mix proportions

The raw materials include Type I Portland cement (C), fly ash, TiO_2 nanoparticles (Aeroxide P25, average diameter: 21 nm), finely ground silica sand (F75, average diameter: 75 μm), PVA fibers, and tap water. Two types of fly ash were investigated, which are Class C fly ash and Class F fly ash, respectively designated as FAC and FAF. The chemical and physical properties of the cement and fly ashes are listed in Table 1. The FAC had a higher calcium content than the FAF. The TiO_2 nanoparticles are composed of 81% anatase and 19% rutile. The PVA fiber (Kuraray Co. Ltd) has a surface oil coating of 1.2% by weight; the properties of the PVA fibers are shown in Table 2.

Seven mix proportions are tested, as listed in Table 3. Four levels of TiO_2 content (0, 1%, 5%, and 10%) were investigated using four mixtures (T0-FAC-2.2, T1-FAC-2.2, T5-FAC-2.2, and T10-FAC-2.2). The mixture T0-FAC-2.2 did not contain any TiO_2 and had a fly ash to cement mass ratio of 2.2; it was used as the reference mixture in this study. Four mixtures (T5-FAC-0.0, T5-FAC-1.0, T5-FAC-2.2, and T5-FAF-2.2) with 5% TiO_2 content were designed to investigate the role of fly ash content and type on PC behavior. A polycarboxylate-based superplasticizer (SP) was used to modify the flowability. The SP content was determined to ensure a consistent mini-slump flow of 165 mm ± 5 mm by flow table test [36]. The PVA fiber content was set at 2% by volume of the mixture. Except the fiber content, other ratios in Table 4 are all by mass.

2.2. Specimen preparation and test procedures

Dry ingredients (cement, fly ash, TiO_2, and sand) were mixed in a Hobart mixer (volume capacity: 19 L) at 1 rps for 5 min, followed by introducing the mixing water and superplasticizer and mixing at 2 rps for another 5 min. Finally, PVA fibers were manually added to the mixer and mixed at 2 rps for another 5 min. After mixing, the mixture was examined by hand, and no fiber agglomeration was found.

The fresh mixture was used to cast plate specimens that measured 76.2 mm × 304.8 mm × 12.7 mm for NO_x abatement testing. Cube specimens that measured 50 mm × 50 mm × 50 mm with no PVA fiber were prepared for microstructure and element characterization. Immediately after casting, the material in mold was covered using a plastic sheet. The specimen was cured in mold for 24 h, and then demolded and cured in air at a relative humidity of 25% ± 5% at 20 °C ± 1 °C for 28 days. The bottom and side surfaces of each plate specimen were sealed using epoxy, only expos-

Table 1
Chemical composition and physical properties of cement and fly ash.

Composition or property	Cement	FAC	FAF
SiO_2 (%)	19.51	38.35	46.09
Al_2O_3 (%)	3.19	17.37	23.15
Fe_2O_3 (%)	2.93	7.88	19.48
CaO (%)	63.50	24.01	5.08
MgO (%)	2.90	3.86	0.77
SO_3 (%)	4.23	3.30	1.12
Na_2O (%)	0.07	1.23	0.58
K_2O (%)	0.76	1.20	1.73
TiO2 (%)	0.28	1.84	–
Loss of ignition (%)	2.60	0.88	1.99
Density (g/cm^3)	3.15	2.71	2.58

Table 2
Manufacturer-specified properties of the PVA fibers.

Length (mm)	Diameter (μm)	Density (kg/m^3)	Young' Modulus (GPa)	Tensile Strength (MPa)	Elongation (%)
12	39	1300	42.8	1600	6

Table 3
Mix proportions*

Designation	C	FAC	FAF	TiO_2/B	W/B	S/B	SP	Fiber (vol.%)
T0-FAC-2.2	1	2.2	0.0	0.00	0.25	0.36	0.006	2
T1-FAC-2.2	1	2.2	0.0	0.01	0.25	0.36	0.011	2
T5-FAC-2.2	1	2.2	0.0	0.05	0.25	0.36	0.029	2
T10-FAC-2.2	1	2.2	0.0	0.10	0.25	0.36	0.059	2
T5-FAC-0.0	1	0.0	0.0	0.05	0.25	0.36	0.060	2
T5-FAC-1.0	1	1.0	0.0	0.05	0.25	0.36	0.034	2
T5-FAC-2.2	1	2.2	0.0	0.05	0.25	0.36	0.029	2
T5-FAF-2.2	1	0.0	2.2	0.05	0.25	0.36	0.044	2

*'B' stands for the sum of cement, fly ash, and TiO_2; 'W' stands for water; 'S' stands for sand.

Table 4
Summary of model parameters determined using the experimental data.

TiO_2 content (%)	Q (L/s)	V (L)	A (1)	B (s)	Y_0 (1)	K ($\times 10^{-3}$ s^{-1})	R^2
0	1/60	35	0.070	1000	0.930	1.00	0.900
1	1/60	35	0.816	500	0.184	1.97	0.998
5	1/60	35	0.948	91	0.052	10.37	0.997
10	1/60	35	0.970	111	0.030	9.99	0.996

ing the top surface to chamber air containing NO_x. The plate specimens were pre-illuminated under UV lamps (10 W/m^2) for 48 h to remove dirt potentially existing on the surface of specimen.

The dispersion of the TiO_2 nanoparticles in the mixtures T1-FAC-2.2, T1-FAC-2.2, T5-FAC-2.2, and T10-FAF-2.2 was examined using the scanning electron microscopy (SEM) and energy dispersive X-ray spectroscopy (EDX) mapping. The samples were prepared in two steps: (1) cut a 10-mm cube from the surface of the cubic specimen, and (2) coat the sample with a thin layer of carbon conducting film by evaporation, to prevent the accumulation of static electric fields at the specimen. Microscopic analysis was conducted using a SEM instrument (model: FEI Nova NanoSEM 450) with an accelerated voltage of 15 kV. The mapping time was 15 min for each EDX scan. Mercury intrusion porosimetry measurements (MIP) was used to characterize the pore structures of matrix of all mixes. To avoid the boundary heterogeneity, inner parts of the cubic specimens were taken and split into particles of 1.5–3 g for MIP test. The maximum pressure that can be applied by the MIP instrument (model: Autopore IV 9500 V1.09) was 45.0 ksi (310 MPa), corresponding to a minimum detectable pore diameter of 4 nm. The contact angle between mercury and hardened ECC matrix was chosen as 130°; the surface tension of mercury was 480 mN/m. A pH meter (accuracy: 0.01) was used to measure the pH of the specimens according to [37,38].

Tensile properties of TiO_2-ECC with different TiO_2 dosage (0, 1%, 5%, and 10%) were tested at 28 days using a uniaxial tensile set-up, as shown in Fig. 1(a). Two LVDTs were used to measure the elongation of the specimen within the gauge length (about 80 mm).

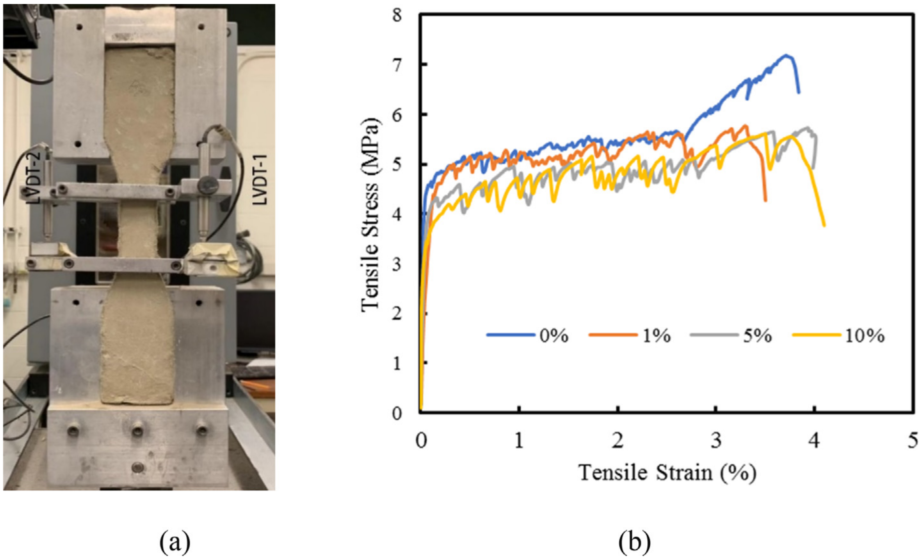

(a) (b)

Fig. 1. Tensile test: (a) set-up; (b) tensile stress–strain curves of TiO_2- doped ECC.

The gauge length was measured using a caliber with an accuracy of ±0.5 μm. Fig. 1(b) shows the representative tensile stress–strain curves of the specimens. The TiO_2-doped ECC retained the strain-hardening properties and high tensile ductility. The tensile strain capacity is around 4%. Details about the specimen preparation, curing, and test procedures are elaborated in [39].

3. Experimental setup and reaction model

3.1. Experimental setup

The NO_x conversion efficiency is typically evaluated using dynamic and static tests [40–42]. In a dynamic test, NO gas is input to a chamber with specimens at a constant flow rate; the NO_x concentration is continuously measured in real time [40]. In a static test, a certain volume of NO gas is input to a chamber and recirculated as a closed circuit in the reaction chamber [41]. Compared with the static test, the dynamic test is more representative for real-world conditions where pollutant gases flow with air [42], and it is thus used in this study.

Fig. 2 shows the PC test set-up, including the gas supply, two flow meters, a gas mixing chamber, a continuously stirred tank reactor (35 L), two UV lamps (model: Philips, power: 15 W) and a chemiluminescent NO_x analyzer (model: ECO PHYSICS CLD 64). An electric fan which provides a constant velocity of 4 m/s, was used for circulating the gas in the reactor. By using the fan for continuous stirring, the gas in the tank reactor is considered uniformly mixed [43,44]. In other words, different areas of the specimen are exposed to the same NO_x concentration [45]. The UV lamps were positioned facing the top surface of the specimens, with a vertical distance of 20 cm between the lamps and specimens. The UV lamps emits UVA irradiation and the light intensity on the surface of specimen was 20 W/m^2, measured using a digital radiometer with a UV sensor.

The inlet gas contained 10 ppm NO (Airgas Inc, US), using N_2 as the balance gas. Pressurized air was used to dilute the NO from 10 ppm to 1 ppm in the mixing chamber. Concentrations of NO, NO_2, and the sum of these, nitrogen oxides (NO_x), were continuously measured using a chemiluminescence NO_x analyzer during the test. The flow rate (1 L/min) and the initial concentration (1 ppm NO_x) were achieved by controlling the flow meters. In the reactor, the relative humidity was 30% ± 2%; the temperature was 20 °C ± 2 °C; and the pressure was 1 atm. Before each PC test, a NO_x flow over the specimens was sustained for 2 h in darkness until reaching a stable 1 ppm concentration, to saturate the adsorption of NO_x by the container and the specimens. This procedure assures that the measured concentration change is exclusively related to the PC reactions, rather than absorption by the sample or container [10].

3.2. Photocatalytic reaction model

The Langmuir-Hinshelwood model was used to describe the PC abatement reaction of NO_x [46]. When the concentration of pollutants is low, the PC reaction followed the first-order kinetics [47–49]. Due to the low initial NO_x concentration (1 ppm) in this study, the first-order reaction model that considers the inlet and outlet gas is used to describe the NO_x abatement reactions, as shown in Eqn. (1).

$$QC_0 - QC - kCV = \frac{dC}{dt} \cdot V \tag{1}$$

where Q (unit: L/s) is the flow rate; C_0 (unit: ppm) is the initial NO_x concentration in the reactor; C (unit: ppm) is the NO_x concentration at time t; k is the reaction rate; V (unit: L) is the volume of the reactor.

Integrating Eq. (1) over time gives Eq. (2):

$$\frac{C}{C_0} = exp\left(-\frac{t}{B}\right) + Y_0 \tag{2}$$

where A, B, and Y_0 are model parameters that are functions of Q, V, and k, as shown below.

$$A = 1 - \frac{Q}{Q + kV}, \quad B = \frac{V}{Q + kV}, \quad Y_0 = \frac{Q}{Q + kV}$$

where A and B characterize the exponential decay of NO_x concentration in the reactor; Y_0 is a dimensionless residual concentration index that represents the ratio of residual NO_x concentration to the initial concentration in steady state (for large values of t). Therefore, η determined from Eqn. (3) represents the PC efficiency that describes the percentage of reacted NO_x. For a specific reaction with fixed flow rate (Q) and volume (V), the reaction rate (k) can be determined through regression analysis using experimental data of $C(t)$.

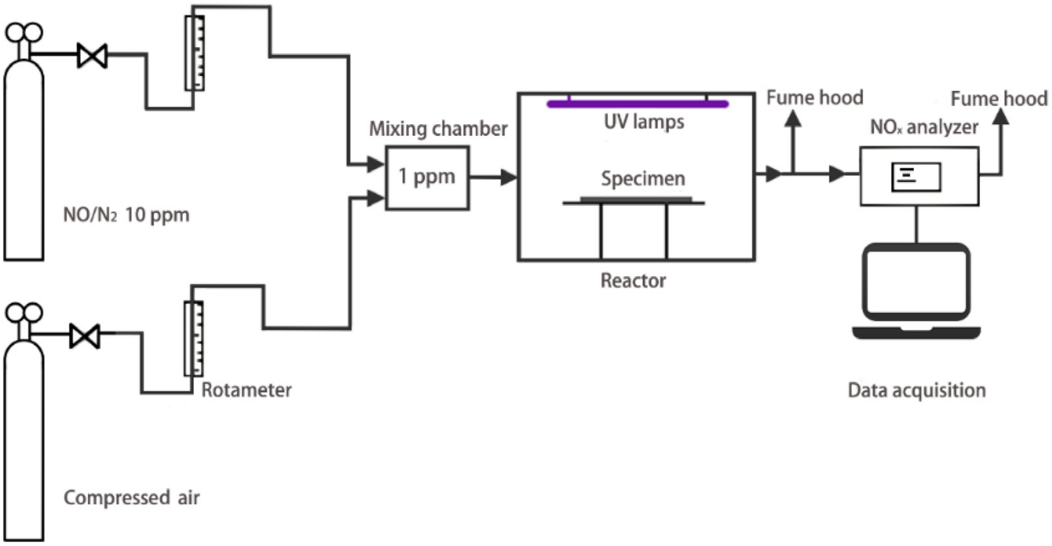

Fig. 2. Experimental setup for the NO_x abatement test.

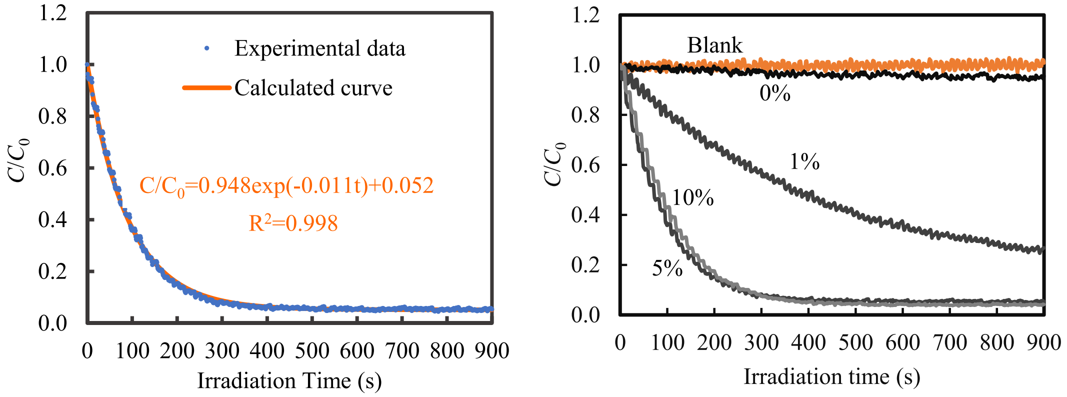

(a) (b)

Fig. 3. Experimental data: (a) the relationship between C/C_0 and the irradiation time (t) shows that the proposed first-order reaction model fits the experimental data of NO_x abatement from T5-FAC-2.2; (b) the experimental results from the specimens with different TiO_2 contents reveal that the NO_x abatement rate (k) and efficiency are dependent on the TiO_2 content.

$$\eta = (1 - Y_0) \times 100\% \tag{3}$$

4. Results and discussions

4.1. NO_x abatement

In this study, the reaction rate k was determined using the PC reaction data from the test of NO_x abatement. In the experiment, $Q = 1/60$ L/s; $V = 35$ L. Fig. 3 shows the experimental results of NO_x concentration ($C(t)$) over the test time up to 900 s (15 min). Fig. 3(a) compares the experimental and fitted curves (using Eqn. (2)) for the mixture T5-FA1-2.2. The coefficient of determination (R^2) is 0.998, indicating a good agreement. Fig. 3(b) compares the test results from specimens (T0-FA1-2.2, T1-FA1-2.2, T5-FA1-2.2, and T10-FA1-2.2) with different TiO_2 contents. As the TiO_2 content is increased from 0% to 5%, NO_x concentration decreases rapidly; however, as the TiO_2 content is increased from 5% to 10%, there is no significant difference between the two curves. The regression analysis results of the model parameters are summarized in Table 4. The coefficient of determination (R^2) is no less than 0.900, indicating that the proposed model fits well with the experimental data for different levels of TiO_2 content.

The results of k and Y_0 are plotted in Fig. 4. Fig. 4(a) shows the effect of TiO_2 content on the reaction. As the TiO_2 content is increased from 0% to 5%, the reaction rate of NO_x concentration is increased approximately linearly from 0.001 to 0.01 s^{-1}; Y_0 is rapidly reduced from 0.930 to 0.052. As the TiO_2 content is increased from 5% to 10%, the reaction rate is slightly reduced; Y_0 is reduced to 0.03. The results suggest that the reaction rate and efficiency become stabilized as the TiO_2 content reaches 5%, which is taken as the saturation content. This is consistent with the observations in other studies [10,50]. Fig. 4(b) shows the effect of fly ash content and type on the reaction. As the fly ash to cement ratio is increased from 0 to 2.2, the reaction rate is increased from 0.003 s^{-1} to 0.010 s^{-1} with an increasing rate (slope); Y_0 is reduced from 0.11 to 0.07. Replacing FA1 with FA2 further increases the reaction rate and reduces the residual NO_x concentration. The underlying mechanisms are investigated in the following sections.

4.2. Dispersion of TiO_2 nanoparticles

The morphology and dispersion of Ti element in the mixtures with different TiO_2 contents are shown in Fig. 5, where Ti element is shown in red color and other elements are shown in black color. Element mapping images show that the dispersion of TiO_2 nanoparticles was reasonably uniform in the mixtures. The dark zones in Fig. 5(f) and 5(h) were occupied by fly ash particles marked by circles. As the TiO_2 content is increased from 0% to 5%, the density of Ti increases, as indicated by the increased brightness of the images; however, as the TiO_2 content is increased from 5% to 10%, the brightness is not significantly changed. Overall, the change of brightness is consistent with the change of reaction rate and PC efficiency (see Fig. 4(a)).

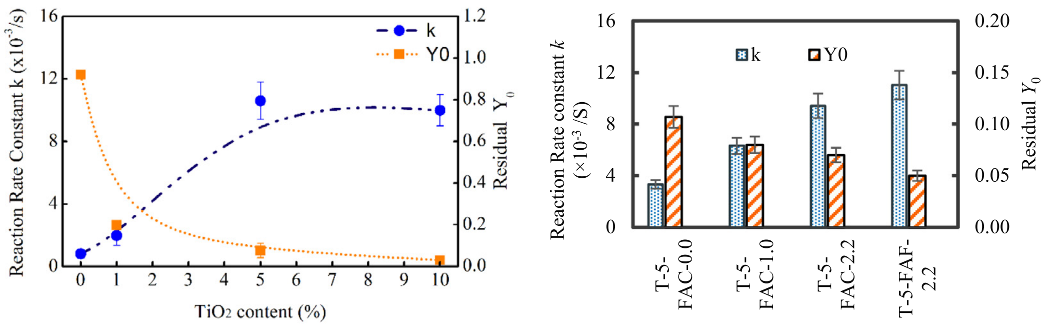

(a) (b)

Fig. 4. The reaction rate and residual NO_x concentration are dependent on: (a) the TiO_2 content, with fixed FAC content at FA/C = 2.2; (b) the fly ash content and type, with fixed TiO_2 content at 5% (variability is within 10%).

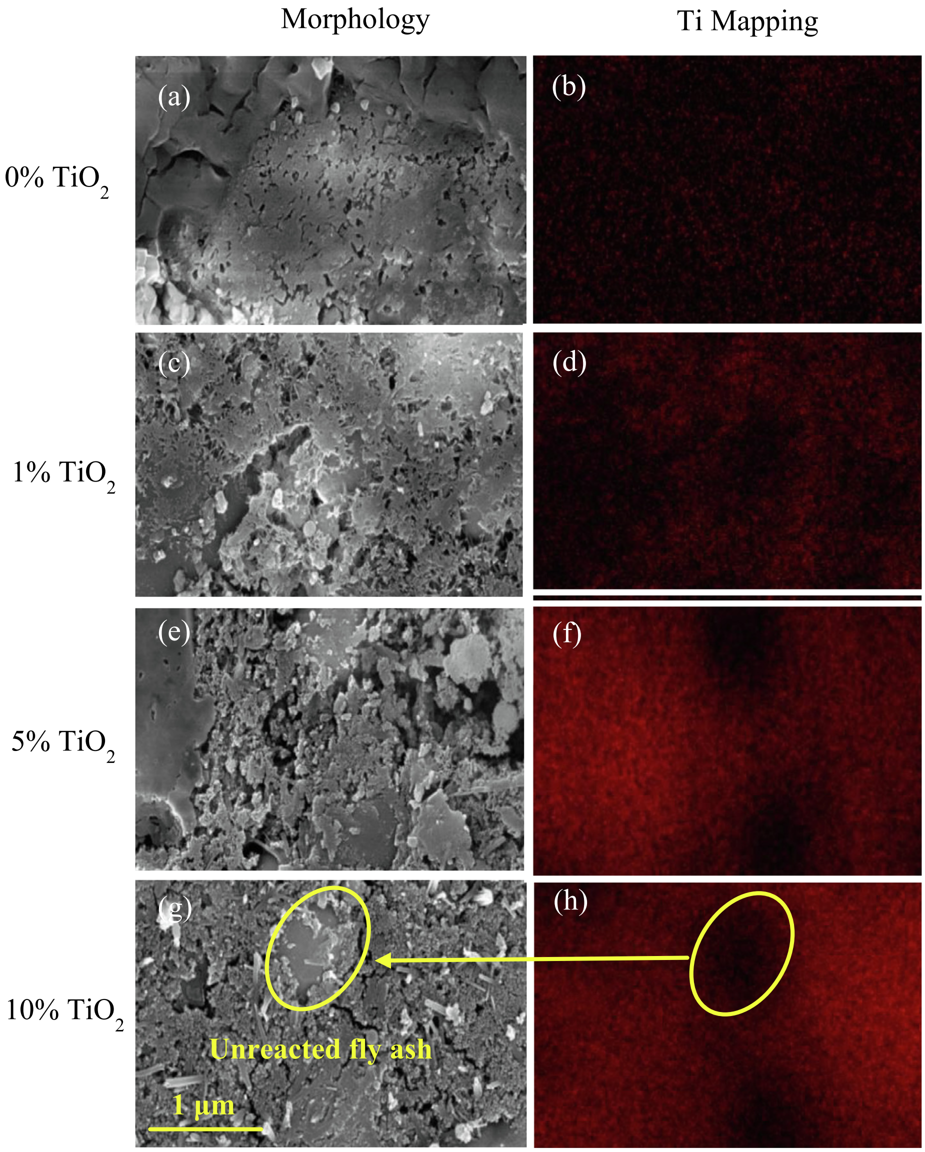

Fig. 5. SEM and EDS images scanned map of the mixtures T0-FAC-2.2, T1-FAC-2.2, T5-FAC-2.2, and T10-FAC-2.2: (a) SEM image of T0-FAC-2.2 (10,000 ×); (b) EDS image corresponding to (a); (c) SEM image of T1-FAC-2.2 (10,000 ×); (d) EDS image corresponding to (c); (e) SEM image of T5-FAC-2.2 (10,000 ×); (f) EDS image corresponding to (e); (g) SEM image of T10-FAC-2.2 (10,000 ×); (h) EDS image corresponding to (g). The red color represents Ti element.

The increase of TiO_2 content from 0% to 5% helps produce more active hydroxyl radicals on the surface of ECC under the same UV irradiation, thus increasing the reaction rate and efficiency. However, further increasing the TiO_2 content beyond 5% has limited influence on the reaction rate and the PC efficiency. The existence of optimal TiO_2 content was also reported in [10,50,51]. Based on the mapping results in this paper, the TiO_2 saturation over 5% on specimen's surface could possibly be the reason for the limited influence of excessive TiO_2 on NO_x abatement. When 5% TiO_2 is applied in ECC, the TiO_2 nanoparticles are supposed to fully occupy ECC's available surface except the smooth surface of fly ash particles. When over 5% TiO_2 is used, the excessive nanoparticles have no space to embed on specimen's surface illuminated by UV light and therefore fail to contribute to the photocatalytic reaction. Other than that, increasing the TiO_2 content from 5% to 10% may lead to agglomeration of the TiO_2 nanoparticles. Agglomeration has adverse effect on the dispersion of the TiO_2 nanoparticles in the matrix. One thing to note is that the 5% TiO_2 content is only optimum for the particular mix composition in this paper. The microstructure or chemical environment of the TiO_2 embedded matrix could also affect the photocatalytic reaction and result in other optimum content.

4.3. Pore characteristics

Fig. 6(a) and (b) show the cumulative pore volume and pore size distribution of the mixtures (T5-FAC-0.0, T5-FAC-1.0, T5-FAC-2.2, and T5-FAF-2.2) with different fly ash contents and types at 28 days. As the fly ash to cement ratio is increased from 0 to 2.2, the cumulative pore volume is increased by about 110%; the pore diameter corresponding to the peak is sustained at about 12 nm, suggesting that adding fly ash increases the porosity, but does not significantly affect the pore size. Since the fly ash is less reactive than the cement, as more fly ash is used to replace the cement, less hydration products are produced, thus increasing the porosity [33]. Replacing FAC with FAF further increases the porosity, and does not affect the pore size distribution. This is consistent with the calcium content that is lower in FAF than that in FAC. The lower

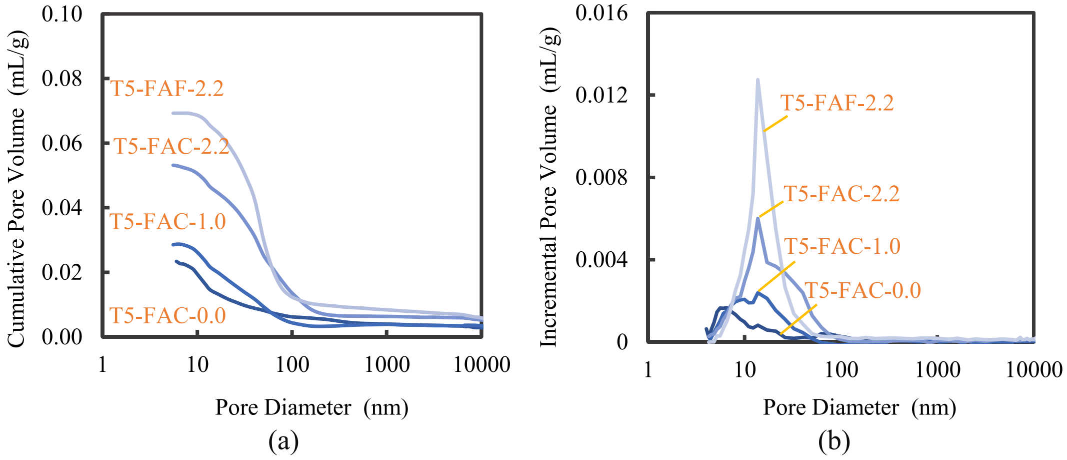

Fig. 6. Pore characteristics: (a) cumulative pore volume increases with fly ash content and its calcium content; (b) pore size distribution does not change with the fly ash content or type.

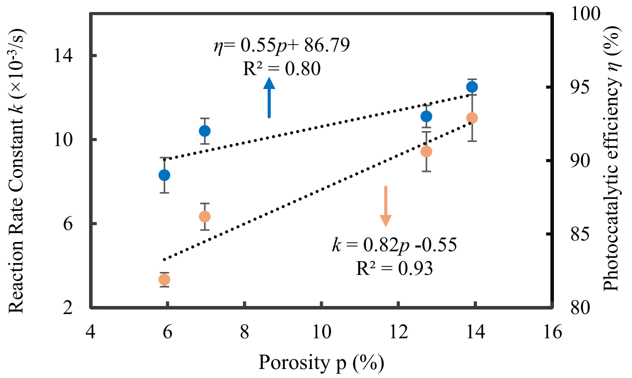

Fig. 7. Experimentally deduced PC reaction rate constant (k), photocatalytic efficiency (η) versus the porosity (p) of the matrix of PC-ECC with different fly ash contents/types, showing a strong correlation between PC reaction rate, efficiency with matrix porosity.

calcium content makes FAF less reactive than FAC, leading to a more porous matrix [52,53].

Fig. 7 shows the plots of reaction rate and photocatalytic efficiency of the mixtures (T5-FAC-0.0, T5-FAC-1.0, T5-FAC-2.2, and T5-FAF-2.2) against the porosity. As the content and type of fly ash change, the porosity increases approximately linearly with the trend of the reaction rate and photocatalytic efficiency. The different data points correspond to the four mixtures, respectively. The correlation in Fig. 7 suggests that the increase of porosity around 12 nm favors the photocatalytic reaction, both in the aspects of the reaction rate and efficiency. Based on Lucas et al.'s finding, the photocatalytic activity can be enhanced by higher porosity if not accompanied by the prevalence of nanopores [10]. However, Folli et al. found that the nano-size internal pores still provide effective surface for TiO_2 in the gaseous pollutant abatement [54]. The size of NO_x is in the order of 1 Å, below 1 nm. Therefore, the TiO_2 embedded on the surface of pores of 12 nm close to the specimen's surface is still active for photocatalytic abatement of NO_x. In this way, the increase of porosity mainly with diameter of 12 nm provides more sites for TiO_2 nanoparticles to embed and more hydroxyl radicals can be produced close to the surface of the specimen to accelerate the reaction rate and enhanced the photocatalytic efficiency.

Based on the experimental results, a schematic model is presented to help understand the PC reactions in the PC-ECC under UV irradiation, as shown in Fig. 8. Hydroxyl radicals ($\cdot OH$) are produced, around the TiO_2 nanoparticles exposed to UV light; the

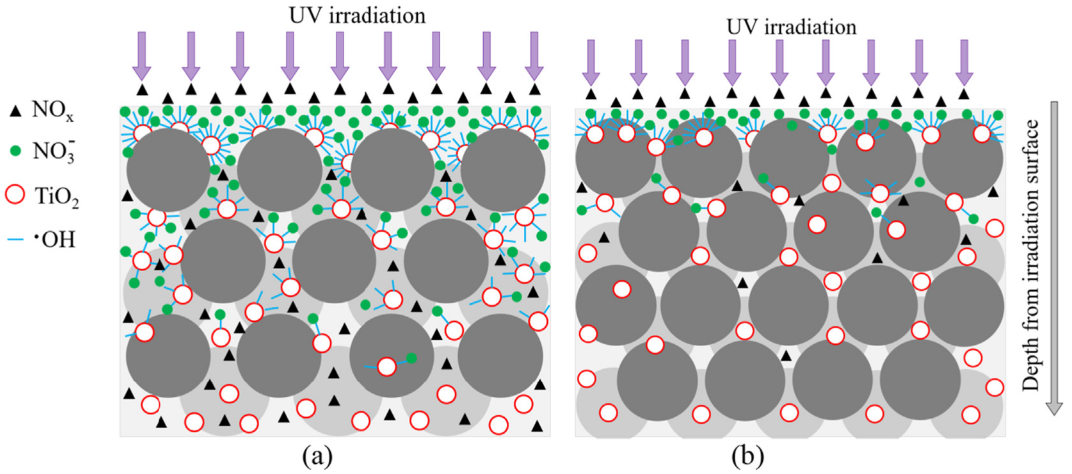

Fig. 8. Schematic diagram showing the porous structure of ECC matrix: (a) a more porous microstructure provides more surface for PC reactions; (b) a less porous microstructure provides less surface for PC reactions. Grey circles represent the hydration products in the hardened ECC matrix; the space between the grey circles represents pores.

Table 5
Results of pH values.

Designation	Mean	COV
T0-FAC-2.2	12.70	0.24%
T1-FAC-2.2	12.67	0.08%
T5-FAC-2.2	12.65	0.24%
T10-FAC-2.2	12.58	0.40%
T5-FAC-0.0	12.84	0.16%
T5-FAC-1.0	12.71	0.08%
T5-FAC-2.2	12.65	0.24%
T5-FAF-2.2	12.66	0.16%

hydroxyl radicals convert NO_x into NO_3^-. The intensity of UV light attenuates with depth from irradiated surface of the matrix. Thus, the hydroxyl radicals are concentrated at the exterior surface of the specimen. When TiO_2 content is constant, as the porosity is increased, more TiO_2 nanoparticles are exposed to UV irradiation, and more water molecules are in contact with the TiO_2 nanoparticles, thus producing more hydroxyl radicals; at the same time, increasing concentrations of hydroxyl radicals enhances reactions with NO_x, promoting the PC efficiency.

4.4. Chemical environment

The pH measurement results of the ECC mixtures are summarized in Table 5. As the TiO_2 content is increased from 0% to 10%, the mean pH value is reduced from 12.70 to 12.58; the corresponding hydrogen ion concentration is increased from 0.1995 pmol/L to 0.2630 pmol/L (by 32%). The reduction of pH value is consistent with the fact that the TiO_2 nanoparticles are not reactive and dilute the cementitious materials that contribute to increasing the pH value in the mixture. As the fly ash to cement ratio is increased from 0 to 2.2, the mean pH value is reduced from 12.84 to 12.65; the corresponding hydrogen ion concentration is increased from 0.1445 pmol/L to 0.1995 pmol/L (by 38%). The reduction in pH value is consistent with the lower calcium content in the fly ash than that in the cement. It was found that a highly alkaline environment is beneficial for the NO_x abatement [24,25,55], because acidic products are produced in the reactions. However, in this study, the reduction of pH value due to the addition of the TiO_2 nanoparticles or the fly ash did not result in a reduction in the reaction efficiency, possibly due to the relatively lower effect of pH compared with the other effects investigated in this research.

5. Conclusions

Based on the experiments in this study, the following conclusions can be drawn.

- TiO_2 in ECC is effective in NO_x abatement. As the TiO_2 content is increased from 0% to 5%, the reaction rate of NO_x abatement increases approximately linearly from 0.001 to 0.01 s^{-1} (Class C fly ash to cement ratio = 2.2). Correspondingly, the residual concentration index is reduced from 0.930 to 0.052. However, a saturation level of TiO_2 content is found for the tested PC-ECC, at 5%. As the TiO_2 content is increased from 5% to 10%, no significant change in the PC efficiency is observed.
- Increasing fly ash content is found to enhance the NO_x abatement efficiency, for a given TiO_2 content. As the Class C fly ash to cement ratio is increased from 0 to 2.2, the reaction rate is increased from 0.003 s^{-1} to 0.010 s^{-1} (at fixed TiO_2 content of 5%); the residual concentration index is reduced from 0.11 to 0.07. Replacing the Class C fly ash with Class F fly ash with low calcium content further increases the reaction rate and efficiency.
- The improvement in NO_x abatement efficiency with increase in fly ash content is found to be associated with microstructure modification – specifically the increase in cumulative pore volume. As the Class C fly ash to cement ratio is increased from 0 to 2.2, the cumulative pore volume is increased by about 110%; the pore diameter corresponding to the peak is sustained at about 12 nm, suggesting that adding fly ash increases the porosity, but does not significantly affect the pore size. Replacing the Class C fly ash with Class F fly ash tends to increase the porosity, thus resulting in a higher reaction rate and PC efficiency.
- With a sustained pore size distribution, increasing the porosity led to increase of PC reaction rate and efficiency. This is consistent with the increase of the TiO_2 surface area, i.e. available reaction sites, exposed to UV light and NO_x.
- For the investigated ranges of TiO_2 content and fly ash content, the pH value did not demonstrate significant effect on the PC efficiency of the ECC mixture, possibly due to the relatively small change range of the pH value, compared with the change of TiO_2 distribution and microstructure of the matrix.
- The first-order reaction model was found to effectively capture the NO_x abatement through PC reactions. The model fit the test data with a coefficient of determination higher than 0.90. The model parameters can be used to evaluate the PC efficiency of TiO_2-doped ECC for air purification.

Declaration of Competing Interest

The authors declare that they have no known competing financial interests or personal relationships that could have appeared to influence the work reported in this paper.

Acknowledgements

Mingfeng Xu greatly appreciates the support provided by China Scholarship Council (CSC) during her visit in the ACE-MRL at the University of Michigan, the National Natural Science Foundation of China (51608382) and the Natural Science Foundation of Shanghai of China (17ZR1442000). This study is partially supported by the James R. Rice Distinguished University Professorship of Engineering at the University of Michigan.

References

[1] S. Guo, M. Hu, M.L. Zamora, J. Peng, D. Shang, J. Zheng, et al., Elucidating severe urban haze formation in China, Proc. Natl. Acad. Sci. 111 (2014) 17373–17378.
[2] Health Effects Institute, State of global air, Boston, MA: Health Effects Institute, 2018.
[3] R. Zhang, A. Khalizov, L. Wang, M. Hu, W. Xu, Nucleation and growth of nanoparticles in the atmosphere, Chem. Rev. 112 (2011) 1957–2011.
[4] J.H. Seinfeld, S.N. Pandis, Atmospheric Chemistry and Physics: From Air Pollution to Climate Change, John Wiley & Sons, 2012.
[5] A. Folli, S.B. Campbell, J.A. Anderson, D.E. Macphee, Role of TiO_2 surface hydration on NO oxidation photo-activity, J. Photochem. Photobiol. A 220 (2011) 85–93.
[6] M.M. Bonato, M.O. Bragança, K.F. Portella, M.E. Vieira, E. Esmanhoto, D.P. Cerqueira, J. Santos, Method for determining the photocatalytic potential of portland cement mortar containing TiO_2 for decomposing the pollutant nitrogen monoxide, Quim. Nova 37 (2014) 1063–1066.
[7] H. Ren, P. Koshy, W.F. Chen, S. Qi, C.C. Sorrell, Photocatalytic materials and technologies for air purification, J. Hazard. Mater. 325 (2017) 340–366.
[8] J. Chen, C.S. Poon, Photocatalytic construction and building materials: from fundamentals to applications, Build. Environ. 44 (2009) 1899–1906.
[9] G. Hüsken, M. Hunger, H. Brouwers, Experimental study of photocatalytic concrete products for air purification, Build. Environ. 44 (2009) 2463–2474.
[10] S.S. Lucas, V.M. Ferreira, J.L.B. de Aguiar, Incorporation of titanium dioxide nanoparticles in mortars - Influence of microstructure in the hardened state properties and photocatalytic activity, Cem. Concr. Res. 43 (2013) 112–120.
[11] D. Wang, Z. Leng, M. Hüben, M. Oeser, B. Steinauer, Photocatalytic pavements with epoxy-bonded TiO_2-containing spreading material, Constr. Build. Mater. 107 (2016) 44–51, https://doi.org/10.1016/j.conbuildmat.2015.12.164.

[12] G.L. Guerrini, E. Peccati, Photocatalytic cementitious roads for depollution, International RILEM symposium on photocatalysis, environment and construction materials, RILEM Florence (2007) 179–186.
[13] T. Maggos, A. Plassais, J. Bartzis, C. Vasilakos, N. Moussiopoulos, L. Bonafous, Photocatalytic degradation of NO_x in a pilot street canyon configuration using TiO_2-mortar panels, Environ. Monit. Assess. 136 (2008) 35–44.
[14] M.M. Ballari, H. Brouwers, Full scale demonstration of air-purifying pavement, J. Hazard. Mater. 254 (2013) 406–414.
[15] M. Pérez-Nicolás, J. Balbuena, M. Cruz-Yusta, L. Sánchez, I. Navarro-Blasco, J.M. Fernández, et al., Photocatalytic NO_x abatement by calcium aluminate cements modified with TiO_2: improved NO_2 conversion, Cem. Concr. Res. 70 (2015) 67–76.
[16] R. Sugrañez, J.I. Álvarez, M. Cruz-Yusta, I. Mármol, J. Morales, J. Vila, et al., Enhanced photocatalytic degradation of NO_x gases by regulating the microstructure of mortar cement modified with titanium dioxide, Build. Environ. 69 (2013) 55–63.
[17] A. Folli, C. Pade, T.B. Hansen, T. De Marco, D.E. Macphee, TiO_2 photocatalysis in cementitious systems: Insights into self-cleaning and depollution chemistry, Cem. Concr. Res. 42 (2012) 539–548.
[18] S. Karapati, T. Giannakopoulou, N. Todorova, N. Boukos, S. Antiohos, D. Papageorgiou, et al., TiO_2 functionalization for efficient NO_x removal in photoactive cement, Appl. Surf. Sci. 319 (2014) 29–36.
[19] Fazhou Wang, Guoxin Sun, Wenqin Zhang, Lu Yang, Peng Liu, Performance of photocatalytic cementitious material: influence of substrate surface microstructure, Constr. Build. Mater. 110 (2016) 175–181, https://doi.org/10.1016/j.conbuildmat.2015.11.030.
[20] T. Sano, N. Mera, Y. Kanai, C. Nishimoto, S. Tsutsui, T. Hirakawa, et al., Origin of visible-light activity of N-doped TiO_2 photocatalyst: behaviors of N and S atoms in a wet N-doping process, Appl. Catal. B-Environ. 128 (2012) 77–83.
[21] B.N. Shelimov, N.N. Tolkachev, O.P. Tkachenko, G.N. Baeva, K.V. Klementiev, A. Y. Stakheev, et al., Enhancement effect of TiO_2 dispersion over alumina on the photocatalytic removal of NO_x admixtures from O_2–N_2 flow, J. Photochem. Photobiol. A 195 (2008) 81–88.
[22] Andrew Mills, Sofia Elouali, The nitric oxide ISO photocatalytic reactor system: measurement of NO_x removal activity and capacity, J. Photochem. Photobiol. A: Chem. 305 (2015) 29–36, https://doi.org/10.1016/j.jphotochem.2015.03.002.
[23] C. Cárdenas, J.I. Tobón, C. García, J. Vila, Functionalized building materials: photocatalytic abatement of NO_x by cement pastes blended with TiO_2 nanoparticles, Constr. Build. Mater. 36 (2012) 820–825.
[24] M. Horgnies, I. Dubois-Brugger, E.M. Gartner, NO_x de-pollution by hardened concrete and the influence of activated charcoal additions, Cem. Concr. Res. 42 (2012) 1348–1355.
[25] N.J. Krou, I. Batonneau-Gener, T. Belin, S. Mignard, M. Horgnies, I. Dubois-Brugger, Mechanisms of NO_x entrapment into hydrated cement paste containing activated carbon — influences of the temperature and carbonation, Cem. Concr. Res. 53 (2013) 51–58, https://doi.org/10.1016/j.cemconres.2013.06.006.
[26] V.C. Li, Engineered cementitious composites (ECC) material, structural, and durability performance, in: E. Nawy (Ed.), Concrete Construction Engineering Handbook, CRC Press, Boca Raton, 2009 (Chapter 24).
[27] V.C. Li, Bendable concrete, innovation in construction, Hong Kong Construction Industry, Council Res. J. (2016) 11–17.
[28] V.C. Li, On engineered cementitious composites (ECC), J. Adv. Concr. Technol. 215–30 (2003).
[29] A. Zhao, J. Yang, E.H. Yang, Self-cleaning engineered cementitious composites, Cem. Concr. Compos. 64 (2015) 74–83.
[30] S. Wang, V.C. Li, Engineered cementitious composites with high-volume fly ash, ACI Mater. J. 104 (2007) 233–241.
[31] E.H. Yang, Y. Yang, V.C. Li, Use of high volumes of fly ash to improve ECC mechanical properties and material greenness, ACI Mater. J. 104 (2007) 620–628.
[32] J. Yu, C.K. Leung, Strength improvement of strain-hardening cementitious composites with ultrahigh-volume fly ash, J. Mater. Civ. Eng. 29 (2017) 05017003.
[33] P. Chindaprasirt, C. Jaturapitakkul, T. Sinsiri, Effect of fly ash fineness on compressive strength and pore size of blended cement paste, Cem. Concr. Compos. 27 (2005) 425–428.
[34] J.K. Tishmack, J. Olek, S. Diamond, S. Sahu, Characterization of pore solutions expressed from high-calcium fly-ash-water pastes, Fuel 80 (2001) 815–819.
[35] B. Lothenbach, K. Scrivener, R. Hooton, Supplementary cementitious materials, Cem. Concr. Res. 41 (2011) 1244–1256.
[36] ASTM C1437-15, Standard Test Method for Flow of Hydraulic Cement Mortar, ASTM International, West Conshohocken, PA, 2015.
[37] G. Plusquellec, M.R. Geiker, J. Lindgård, J. Duchesne, B. Fournier, K. De, Weerdt, Determination of the pH and the free alkali metal content in the pore solution of concrete: review and experimental comparison, Cem. Concr. Res. 96 (Supplement C) (2017) 13–26.
[38] V. Räsänen, V. Penttala, The pH measurement of concrete and smoothing mortar using a concrete powder suspension, Cem. Concr. Res. 34 (2004) 813–820.
[39] Y. Bao, M. Xu, D. Soltan, T. Xia, A. Shih, H.L. Clack, et al., in: Three-Dimensional Printing Multifunctional Engineered Cementitious Composites (ECC) for Structural Elements, Springer, 2018, pp. 115–128.
[40] Japanese Standards Association, Fine ceramics (advanced ceramics, advanced technical ceramics) Test method for air purification performance of photocatalytic materials, part 2: removal of acetaldehyde, 2004.
[41] T. Maggos, J. Bartzis, P. Leva, D. Kotzias, Application of photocatalytic technology for NO_x removal, Appl. Phys. A-Gen. 89 (2007) 81–84.
[42] A.R. Jayapalan, B.Y. Lee, E.M. Land, M.H. Bergin, K.E. Kurtis, Photocatalytic efficiency of cement-based materials: demonstration of proposed test method, ACI Mater. J. 112 (2015).
[43] S. Ifang, M. Gallus, S. Liedtke, R. Kurtenbach, P. Wiesen, J. Kleffmann, Standardization methods for testing photo-catalytic air remediation materials: Problems and solution, Atmos. Environ. 91 (2014) 154–161, https://doi.org/10.1016/j.atmosenv.2014.04.001.
[44] C. Minero, A. Bedini, M. Minella, On the standardization of the photocatalytic gas/solid tests, Int. J. Chem. React. Eng. 11 (2013) 717–732.
[45] A.E. Cassano, C.A. Martin, R.J. Brandi, O.M. Alfano, Photoreactor analysis and design: fundamentals and applications, Ind. Eng. Chem. Res. 34 (1995) 2155–2201.
[46] M. Ballari, M. Hunger, G. Hüsken, H. Brouwers, NO_x photocatalytic degradation employing concrete pavement containing titanium dioxide, Appl. Catal. B-Environ. 95 (2010) 245–254.
[47] I. Arabatzis, N. Spyrellis, Z. Loizos, P. Falaras, Design and theoretical study of a packed bed photoreactor, J. Mater. Process. Technol. 161 (2005) 224–228.
[48] Z. Ai, L. Zhang, S. Lee, Efficient visible light photocatalytic oxidation of NO on aerosol flow-synthesized nanocrystalline $InVO_4$ hollow microspheres, J. Phys. Chem. C 114 (2010) 18594–18600.
[49] Z. Ai, W. Ho, S. Lee, L. Zhang, Efficient photocatalytic removal of NO in indoor air with hierarchical bismuth oxybromide nanoplate microspheres under visible light, Environ. Sci. Technol. 43 (2009) 4143–4150.
[50] F. Toma, G. Bertrand, D. Klein, C. Coddet, Photocatalytic removal of nitrogen oxides via titanium dioxide, Environ. Chem. Lett. 2 (2004) 117–121.
[51] J.M. Herrmann, Heterogeneous photocatalysis: fundamentals and applications to the removal of various types of aqueous pollutants, Catal. Today 53 (1999) 115–129.
[52] V.G. Papadakis, Effect of fly ash on Portland cement systems: part II. High-calcium fly ash, Cem. Concr. Res. 30 (2000) 1647–1654.
[53] V.G. Papadakis, Effect of fly ash on Portland cement systems: part I low-calcium fly ash, Cem. Concr. Res. 29 (1999) 1727–1736.
[54] A. Folli, I. Pochard, A. Nonat, U.H. Jakobsen, A.M. Shepherd, D.E. Macphee, Engineering photocatalytic cements: understanding TiO_2 surface chemistry to control and modulate photocatalytic performances, J. Am. Ceram. Soc. 93 (2010) 3360–3369.
[55] B.Y. Lee, A.R. Jayapalan, M.H. Bergin, K.E. Kurtis, Photocatalytic cement exposed to nitrogen oxides: effect of oxidation and binding, Cem. Concr. Res. 60 (2014).